AIAA JOURNAL
Vol. 37, No. 9, September 1999

Laminar-Turbulent Transition in a Mach 8 Elliptic Cone Flow

Roger L. Kimmel* and Jonathan Poggie†
U.S. Air Force Research Laboratory, Wright–Patterson Air Force Base, Ohio 45433-7521
and
Stephen N. Schwoerke‡
Lockheed Martin Corporation, Fort Worth, Texas 76101-0748

To examine the influence of crossflow on transition in a hypersonic boundary layer, an experimental and computational study was made of a Mach 8 flow over a sharp-nosed elliptic cone of 2:1 cross section. Extensive flow visualization was carried out experimentally, including schlieren photography and surface oil-flow visualization. Mean pressure and heat flux were measured at the wall of the wind-tunnel model. For comparison with the experiments, a computation of the basic state flow was carried out using the parabolized Navier–Stokes equations. The basic state laminar flow was found to be relatively complex, with highly skewed velocity profiles and a pair of symmetric vortices on the top centerline of the cone. Transition in the elliptic cone flow was found to be significantly different than transition in hypersonic flow over planar and axisymmetric configurations, which is driven by the second mode instability. In the elliptic cone flow the transition front was nonuniform, with early transition near the top centerline and delayed transition near the leading edge. Rope waves were observed on both the leading edge and top centerline; unusual elongated streaks were observed on the top centerline. Transition on the top centerline may be related to an instability of the inflectional boundary-layer velocity profiles in that region. A traveling crossflow instability is probably important in the vicinity of the shoulder of the cone, and tentative evidence of a stationary crossflow instability was obtained with the introduction of artificial roughness.

Nomenclature

C_H = Stanton number, $q_w/[\rho_e U_e(h_0 - h_e)]$
f = frequency
h = enthalpy
i, j, k = computational grid indices along the radial, circumferential, and axial directions (Fig. 1)
k = roughness height
L = length of elliptic cone, 1.016 m
M = Mach number
p = pressure
q = heat flux
Re_{cf} = crossflow Reynolds number, $W_{\max}\delta_{10}/\nu_e$
Re_k = roughness Reynolds number, Uk/ν
Re_L = length Reynolds number, $U_\infty L/\nu_\infty$
Re_x = running Reynolds number, $U_\infty x/\nu_\infty$
Re_θ = momentum thickness Reynolds number, $U_\infty\theta/\nu_\infty$
r = ratio of measured heat flux to computed laminar flow heat flux
T = temperature
U = streamwise velocity component
W = crossflow velocity component
x, y, z = streamwise, spanwise, and vertical coordinates (Fig. 1)
δ = boundary-layer thickness (based on $h_0/h_{0\infty} = 1.0008$ in this study)
η = wall-normal coordinate
θ = angle in cylindrical coordinate system (Fig. 1)
ν = kinematic viscosity
ρ = density

Subscripts

e = boundary-layer edge conditions
w = wall conditions
0 = stagnation conditions
∞ = freestream conditions (upstream of shock)

Received 19 May 1998; revision received 2 February 1999; accepted for publication 2 February 1999. This paper is declared a work of the U.S. Government and is not subject to copyright protection in the United States.

*Research Aerospace Engineer, Air Vehicles Directorate, AFRL/VAAA, 2130 Eighth Street, Suite 1. Senior Member AIAA.
†Research Aerospace Engineer, Air Vehicles Directorate, AFRL/VAAC, 2210 Eighth Street, Room 225. Senior Member AIAA.
‡Engineering Specialist, Tactical Aircraft Systems, Mail Zone 2275, P.O. Box 748.

Introduction

Two-Dimensional Boundary Layers

MUCH of the past work on hypersonic boundary-layer stability has focused on the flow over bodies with planar or axial symmetry. The instability mechanisms—if not the receptivity and transition mechanisms—are fairly well understood for this class of flows. If, in the reference frame of a neutral wave, there is supersonic flow over part of the boundary-layer profile, then multiple modes exist.[1,2] The modes are distinguished by their characteristic functions or profiles along the wall-normal direction.

The first mode (vorticity mode) is, for lower supersonic Mach numbers, the compressible flow counterpart of the Tollmien–Schlichting wave. For hypersonic Mach numbers, however, the first mode represents both a viscous Tollmien–Schlichting instability and an inviscid instability because of the presence of a generalized inflection point in the basic state profiles.[3] The most unstable first mode wave is two-dimensional in incompressible flow, but becomes increasingly skewed to the freestream direction as the Mach number increases from zero. The second mode (the first acoustic mode or Mack mode) is also an inviscid instability associated with a generalized inflection point. It has no counterpart in incompressible flow and is unskewed for two-dimensional boundary-layer flows.

Boundary-layer transition is a function of receptivity (response of the boundary layer to external disturbances) and amplification history. As a disturbance of constant frequency propagates downstream in a typical two-dimensional hypersonic boundary layer, a first mode component is initially most amplified, and farther downstream a second mode component is most amplified.[4–6] For experiments in quiet wind tunnels and conventional tunnels with relatively low noise environments, the second mode instability is usually the dominant cause of transition.[7–11] For a relatively lower hypersonic Mach number, however, transition may be dominated by the first mode.[12,13]

Previous experimental work[14,15] has shown that, at least in a conventional wind-tunnel environment, disturbances in the boundary layer extend over a limited streamwise and circumferential distance. Disturbances begin their life as wave packets and evolve toward the coherent structures typically seen in turbulent boundary layers.[16]

For sections parallel to the wall, cross-correlation data suggest that the wave packets appear as elliptical patches traveling in the direction of the freestream flow. In sections perpendicular to the wall, highly inclined structures are seen concentrated near the boundary-layer edge. As the Reynolds number increases, the streamwise and circumferential extent of the disturbances decreases rapidly, and the structures become more erect with greater extent along the wall-normal direction.

Three-Dimensional Boundary Layers

In general, the boundary-layer flow on a three-dimensional body experiences strong lateral pressure gradients that turn the streamlines away from the axial direction. The low momentum fluid closer to the wall experiences greater turning, inducing a skewed boundary-layer velocity profile with a component perpendicular to the local flow direction at the boundary-layer edge. This component is called crossflow. The crossflow velocity component is zero at the wall and in the freestream, and the profile typically has a single maximum toward the middle of the boundary layer and an inflection point somewhat farther from the wall. The inflected crossflow velocity profile exhibits an inviscid instability.

The character of the crossflow instability is well-established for subsonic and moderately supersonic flows over swept wings and for certain model problems, such as rotating disks, cones, and spheres.[17] Corotating vortices form with their axes aligned approximately with the streamwise direction. The spanwise wavelength is on the order of the boundary-layer thickness, and the wave-number vector is typically oriented at large angle to the inviscidflow streamlines. Stability calculations indicate that the most amplified disturbances are typically traveling waves, but experimental results are often dominated by roughness-induced stationary disturbances. Crossflow vortices may undergo a secondary instability process that produces horseshoe vortices.

Relatively few studies of three-dimensional boundary layers have been carried out for hypersonic flow. The experiments have generally been limited to sharp and blunt cones at angle of attack,[18,19] but some data do exist for the elliptic cone geometry.[20] Stability computations[21,22] show some interesting trends: crossflow increases the amplification rate and skewness of the most unstable first mode wave, and the most amplified second mode wave can be oblique to the freestream flow.

The objective of the present investigation was to examine stability and transition on a fully three-dimensional configuration and to demonstrate a case in which a crossflow instability had a significant influence on boundary-layer transition. An elliptic cone was chosen because it should induce significant crossflow, is easily described analytically, and resembles a realistic hypersonic vehicle. The design study for these experiments was documented in a previous paper.[23] The present paper reports results on the overall features of the elliptic cone flow, including surface pressure measurements, surface heat-flux measurements, flow visualization, and a computation of the basic state laminar flow based on the parabolized Navier–Stokes equations. A companion paper[24] reports measurements with hot-film probes, as well as linear stability calculations.

Procedure

Experiments

The experiments were carried out in the von Kármán Gas Dynamics Facility Tunnel B at the Arnold Engineering Development Center. Tunnel B[25–27] is a closed-circuit continuous-run facility with a 1.27-m diam test section. Incoming air is heated with a natural gas combustion heater, and the walls of the entire tunnel are cooled with external water jackets. The facility is equipped with two axisymmetric nozzles that allow the tunnel to be run at a nominal Mach number of either 6 or 8. The present tests were carried out at a measured freestream Mach number of $M_\infty = 7.93$ and a stagnation temperature of $T_0 = 728$ K in the settling chamber. The experimental model was tested under both adiabatic wall and cold wall conditions, as described next.

The freestream flow in Tunnel B has been extensively monitored and calibrated.[27] The mean Mach number on the tunnel centerline is spatially uniform to within 1.2%. The broadband rms mass flux (the disturbance level) on the centerline is between 1.2 and 1.5% of the local mean, depending on the unit Reynolds number. Root-mean-square total temperature fluctuations are an order of magnitude smaller. The freestream disturbance spectrum is similar for all unit Reynolds numbers for both mass flux and total temperature fluctuations. It peaks at a frequency of $f = 2$–3 kHz and drops off for higher frequencies as approximately $1/f$.

The experimental model was a sharp-nosed cone with an elliptical cross section. The nominal nose radius was 40 μm along the major axis. The aspect ratio of the cross sections was 2.0:1, and the cone half-angle was 7 deg in the minor axis. The model was composed of a solid nose section and three hollow frusta, each with a nominal wall thickness of 6.4 mm. The overall length of the model was $L = 1.016$ m. The nose section was 0.1524 m long, the next two frusta were 0.2794 m long, and the final frustum was 0.3048 m long. All four sections were constructed of 17-4 PH stainless steel with better than 0.81 μm rms finish.

The wind-tunnel model and the coordinate systems used in the present paper are illustrated in Fig. 1. A Cartesian coordinate system fixed to the model nose was aligned so that the x axis was along the axial direction. The z coordinate was taken to be vertical, and the y direction was chosen to make the system right-handed. Using a cylindrical coordinate system with $\theta = 0$ deg at the top centerline (minor axis endpoint) and $\theta = 90$ deg at the leading edge (major axis endpoint) was also convenient. The four quadrants were interchangeable because of the symmetry of the model. One quadrant of the model was devoted to pressure instrumentation, and one was devoted to heat transfer (Fig. 2). One entire side was devoid of pressure taps and heat transfer gauges and was devoted to hot-film probe measurements of the boundary layer. Heat-transfer gauges

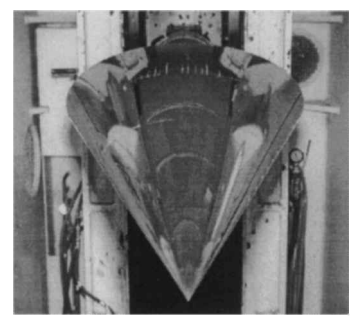

a) Front view of model in tunnel airlock

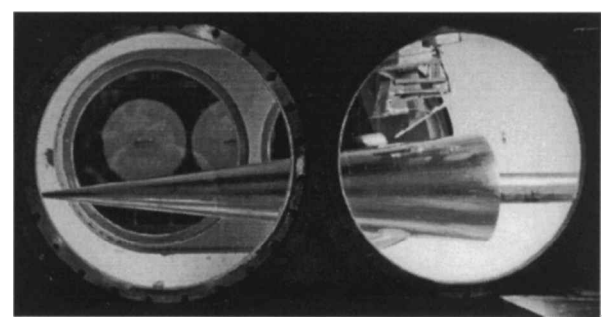

b) Side view of model inside tunnel

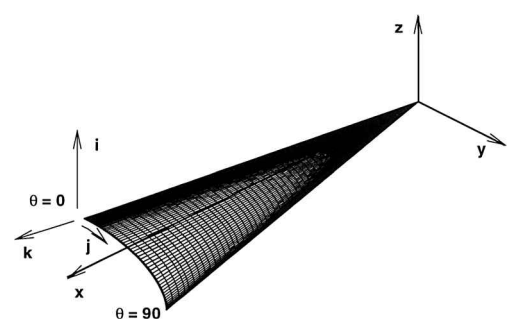

c) Coordinate system

Fig. 1 Model geometry and coordinate system.

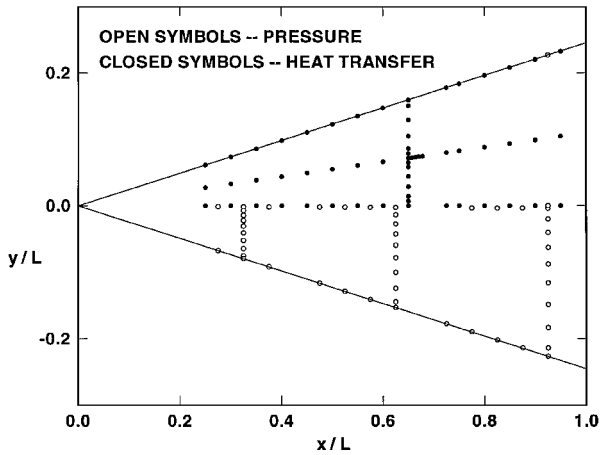

Fig. 2 Locations of pressure taps and heat transfer gauges. Vertical scale is exaggerated for clarity.

and pressure taps near the leading edge of the model were displaced toward the instrumentation side by 2 deg to keep the model leading edges clean.

The pressure taps consisted of 1-mm-inside-diameter stainless-steel tubing, and were arranged in the configuration shown by open symbols in Fig. 2. Pressure surveys were made under near adiabatic wall conditions. Four pressure taps at $x/L = 0.925$ were located on the endpoints of the major and minor diameters. Each pair of diametrically opposed pressure taps was connected to a single transducer. The model angle of attack was adjusted to 0 deg $\pm$ 0.1 deg by nulling the differential pressure for each pair of taps.

The heat-transfer gauges consisted of 4.8-mm diam Schmidt–Boelter gauges and were arranged in the configuration shown by closed symbols in Fig. 2. A Schmidt–Boelter gauge is an aluminum wafer wrapped with constantan wire and half-plated with copper to create a thermopile of 35–40 thermocouple junctions. A constant heat flux to the front surface generates a constant temperature difference across the wafer, which is measured by the thermopile.

Heat-transfer measurements were made for a wall temperature to stagnation temperature ratio of $T_w/T_0 = 0.42$. Both temperatures were monitored continuously during the tests. The stagnation temperature was held fixed by the tunnel heater system, and the model temperature was controlled by the following process. Between runs the model was cooled to room temperature. For each test the model was injected into the tunnel airflow, the output of the Schmidt–Boelter gauges was recorded before any significant increase in the model wall temperature occurred, and the model was retracted from the tunnel. Reynolds numbers based on model length of $Re_L = 1.7 \times 10^6$, 2.0×10^6, 2.7×10^6, 3.3×10^6, 4.0×10^6, 5.0×10^6, 6.0×10^6, and 6.7×10^6 were tested.

Extensive flow visualization studies were carried out under near adiabatic wall conditions. Surface oil-flow patterns were generated by applying a mixture of silicone oil and silicone pigment in lines either along one leading edge or around the circumference of the wind-tunnel model, then injecting the model into the flow and videotaping the flow pattern. Schlieren photographs were also obtained. The wind-tunnel sting mount allowed the model to be rolled at different angles from the viewing direction in order to examine the boundary layer in different planes around the cone.

Numerical Simulations

As part of the design process for this experiment, parabolized Navier–Stokes (PNS) calculations of the basic state laminar flow and linear stability calculations for the disturbance flowfield were carried out for several different elliptic cone configurations.[23] Lyttle and Reed[28,29] obtained very similar results in computations for a 2:1 elliptic cone at Mach 4. The experiments discussed here were carried out under somewhat different test conditions than those modeled in the original design calculations. Some new PNS calculations are presented in this paper for the actual test conditions. Computations were carried out for both the cold wall conditions corresponding to the heat-transfer measurements and the adiabatic wall conditions of the other measurements.

A detailed discussion of the computational modeling of this configuration, including grid resolution studies, was presented in an earlier paper.[23] For brevity, only a short summary of the computational procedure is given here. The basic state computations for the laminar boundary-layer flow were carried out using the upwind scheme (UPS) PNS code, as modified by Lockheed Martin Tactical Aircraft Systems.[30] The code uses a second-order central difference scheme for inviscid fluxes and a fourth-order smoothing model. The outer boundary condition was a shock-fitting model, and the solution for the first 25 mm of the cone was obtained with a Navier–Stokes nose solution code. The computation grid for the nose solution consisted of $121 \times 71 \times 31$ points and the PNS grid was $121 \times 71 \times 875$ points, for both cases distributed over one 90-deg quadrant of the cone along the radial, circumferential, and axial directions, respectively.

To validate the basic state computation, we compared the predicted surface pressures and heat-transfer rates to the experimental data from the laminar flow region on the cone. As will be shown next, the computations agreed with the measured wall pressure and heat flux within the uncertainty in the experimental data.

Results

Wall-Pressure Measurements

To achieve the best possible instrument resolution, wall-pressure measurements were carried out at the highest stagnation pressure, corresponding to $Re_L = 6.7 \times 10^6$. Laminar flow computations were carried out for adiabatic wall conditions at the same Reynolds number. The results are shown in Fig. 3, and the computation is seen to agree with the experiment within 5%, which is approximately the experimental uncertainty.

The circumferential pressure profiles (Fig. 3a) illustrate a fundamental difference between the elliptic cone flow and a typical axisymmetric flow: there is a pronounced rise in pressure along the circumference of the cone between the shoulder ($\theta = 45$ deg) and the leading edge ($\theta = 90$ deg). The data from the three streamwise stations ($x/L = 0.325$, 0.625, and 0.925) lie generally along a common curve, indicating an approximate conical similarity for the inviscid flow between the shock and the boundary-layer edge.

The pressure is nearly uniform along rays of the cone (Fig. 3b), except for a small region near the nose. Rapid growth of the boundary-layer displacement thickness in that region induces slightly increased wall pressures that relax downstream (the viscous interaction effect). The effect is most pronounced near the top centerline ($\theta = 2$ deg) because of the thick boundary layer in that vicinity.

Flow Visualization

The strong circumferential component of the pressure gradient in the elliptic cone flow drives the boundary-layer fluid from the leading edge toward the top centerline. The basic state computations show that the boundary-layer edge streamlines (solid lines in Fig. 4) are driven slightly inboard of the conical rays that would be seen in flow over an axisymmetric cone. The low momentum fluid closer to the wall experiences greater turning, and the limiting surface streamlines (dashed lines in Fig. 4) are highly skewed inboard, converging toward a stable bifurcation line just off the centerline.

Surface oil-flow images were obtained for comparison with the computed wall streamlines. (Wall conditions were between the adiabatic and cold wall reference cases.) Sample oil-flow images are shown in Fig. 5 for $Re_L = 2.0 \times 10^6$. Here the model was rolled so that the top centerline was visible through a side window in the wind tunnel. A mixture of silicone oil and silicone pigment was applied either along one leading edge of the model (Fig. 5a) or in lines around the circumference (Fig. 5b). Oil streaks on the forward one-third of the model, where laminar flow prevailed, show the same pattern as the computed wall streamlines.

Indications of transition appear in the oil-flow pattern in the region toward the top centerline and the aft portion of the model (see Fig. 5b). Oil in a roughly triangular region on the top side of the cone has been dragged farther downstream, indicating higher mean shear stress caused by turbulent flow. The corresponding streaks appear to be roughly aligned with the axial direction, in contrast to the

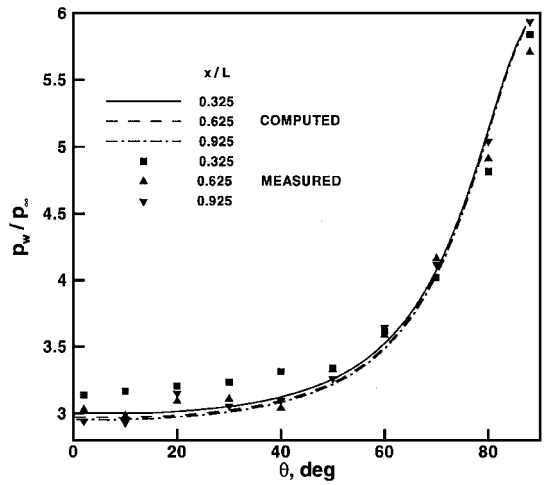

a) Pressure around the circumference

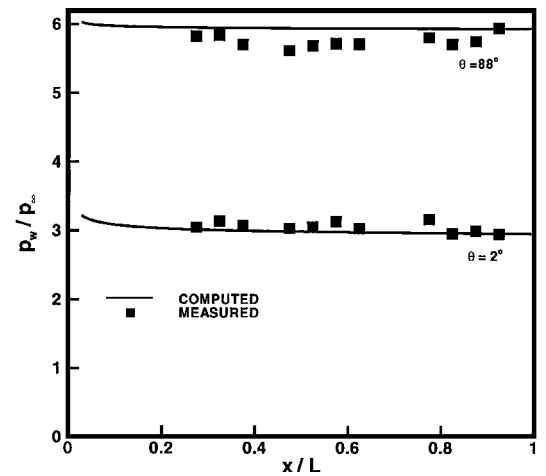

b) Pressure along rays

Fig. 3 Surface pressure distributions.

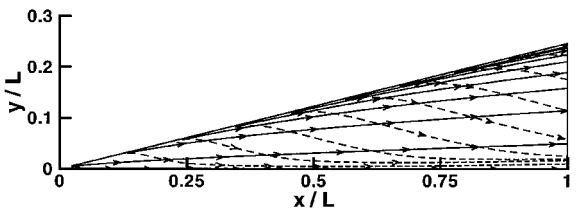

Fig. 4 Plan view of computed streamline patterns for adiabatic wall case at $Re_L = 2.0 \times 10^6$: ——, boundary-layer edge streamlines; and - - -, limiting wall streamlines.

significant skewness seen elsewhere. With the enhanced momentum transport in the wall-normal direction in the turbulent flow region, the magnitude of the crossflow is reduced, and the wall streamlines are more closely aligned with the edge streamlines.

The influx of fluid from around the the model circumference leads to substantial thickening and deceleration of the boundary layer in the vicinity of the centerline on the flat side of the model. Figure 6a shows the computed boundary-layer thickness for different circumferential positions at $x/L = 0.802$. At this streamwise station the boundary-layer thickness at the centerline is about seven times greater than at the leading edge. Boundary-layer profiles also tend to be inflectional in this region, as seen in the examples in Fig. 6b.

Schlieren photographs were taken under approximately adiabatic wall conditions with the model rolled at different angles from the viewing direction in order to examine the boundary layer in different planes around the cone. Three examples are shown in Fig. 7. A

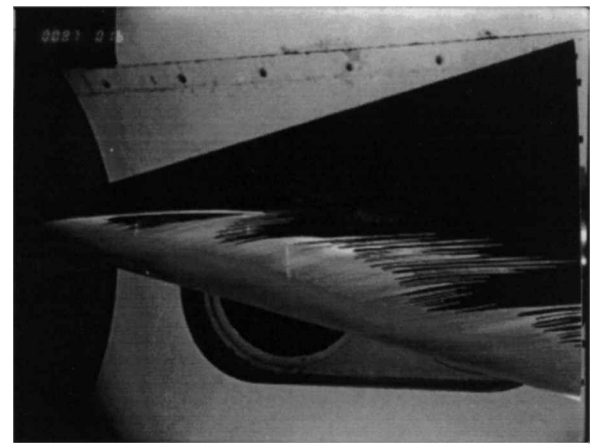

a) Marker material along leading edge

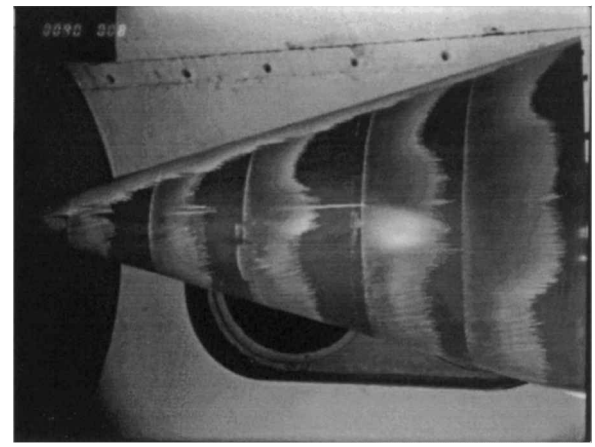

b) Marker material around circumference

Fig. 5 Surface oil-flow visualization for $Re_L = 2.0 \times 10^6$.

3×3 sharpen kernel has been applied to the images to enhance the contrast of features in the boundary layer. A field of view through the wind-tunnel window of about $0.4L$ is visible in each image (see Fig. 1b). The dark triangular region in each image represents the wind-tunnel model, the boundary layer is evident as a light band just above the model, and the shock appears as a slightly wrinkled dark line somewhat farther from the model surface.

Figure 7a is a plan view of the model for $Re_L = 6.7 \times 10^6$. The thin boundary layer in the $\theta = 90$ deg plane is visible in the image, and rope-waves are just discernible. Figure 7b shows an intermediate roll angle, displaying the $\theta = 63$ deg plane for $Re_L = 2.0 \times 10^6$. The increased boundary-layer thickness at this station is evident, and striking elongated streaks are present in the boundary-layer flow, oriented at about 5 deg from the cone surface. The boundary layer appears still thicker in the side view ($\theta = 0$ deg plane visible) at the same Reynolds number shown in Fig. 7c, and the elongated streaks are still present. Farther downstream, structures with wavelengths of roughly 2δ–3δ are visible. Boundary-layer breakdown appears to occur at the rightmost station visible in the image.

Heat-Transfer Measurements

Figure 8 shows profiles of Stanton number vs streamwise Reynolds number for three rays along the surface of the cone. Experimental data and the corresponding cold wall computations are shown for $Re_L = 1.7 \times 10^6$ and 6.7×10^6. We first focus on the portion of the cone where laminar flow prevails. In this regime the experiment and the laminar flow computation agree within the apparent scatter in the experimental data. (Measurements with Schmidt–Boelter gauges in two-dimensional flows typically have an uncertainty of $\pm 10\%$. Greater scatter is apparent in the present data, which were obtained in a complex, three-dimensional flow.) For

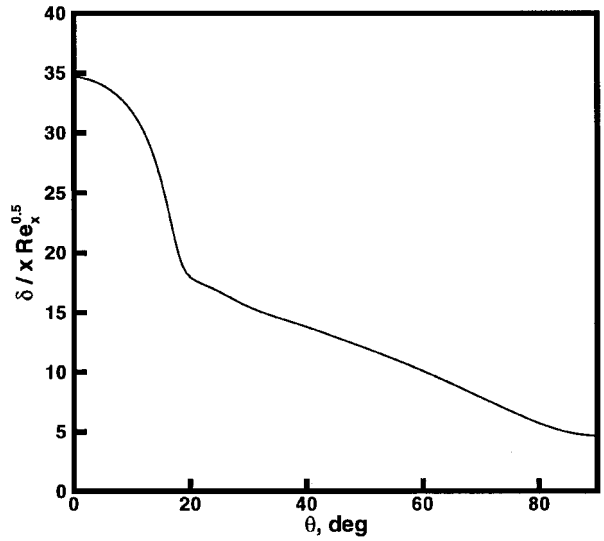

a) Boundary-layer thickness

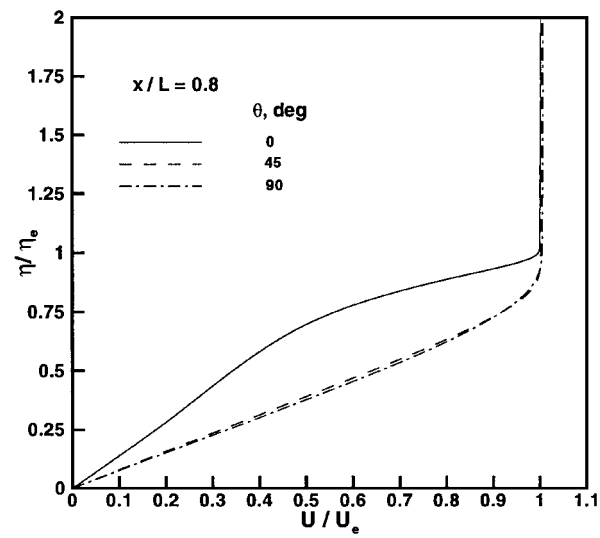

b) Axial velocity component

Fig. 6 Computed conditions at $x/L = 0.802$ for adiabatic wall case at $Re_L = 2.0 \times 10^6$.

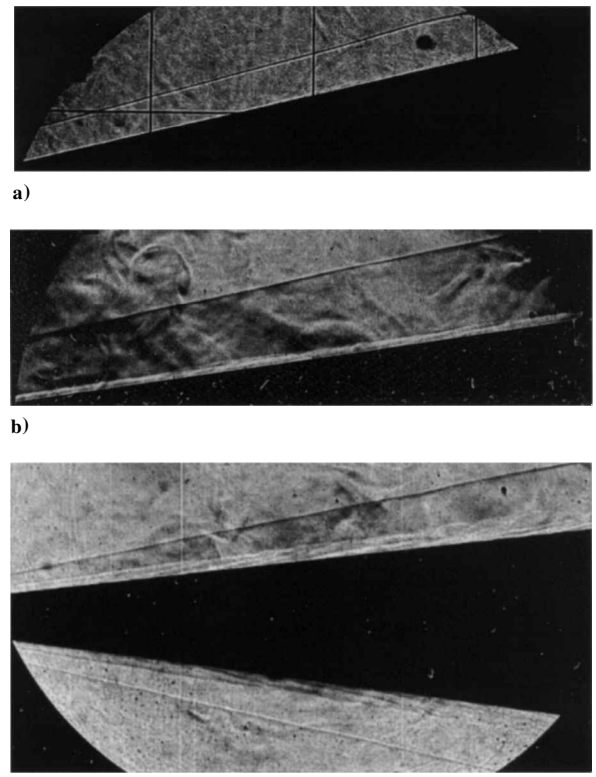

a)

b)

c)

Fig. 7 Schlieren photographs: a) plan view, plane $\theta = 90$ deg visible, $Re_L = 6.7 \times 10^6$, $0.6 \leq x/L \leq 1.0$; b) intermediate view, plane $\theta = 63$ deg visible, $Re_L = 2.0 \times 10^6$, $0.6 \leq x/L \leq 1.0$; and c) side view, plane $\theta = 0$ deg visible, $Re_L = 2.0 \times 10^6$, $0.1 \leq x/L \leq 0.5$.

the rays near the leading edge ($\theta = 88$ deg; Fig. 8a) and along the shoulder ($\theta = 45$ deg; Fig. 8b), the results closely follow the trend: $C_H \propto Re_x^{-1/2}$. This trend is not evident along the top centerline ($\theta = 0$ deg; Fig. 8c), where the boundary-layer profile is thick and inflectional.

Along each ray transition appears in the experimental data as an abrupt rise in the heat-transfer rate and a concomitant departure from the computation. A moderate unit Reynolds number effect on transition location was present, as illustrated in Fig. 8b. The relative stability of the leading edge where transition occurs at $Re_x = 5.5 \times 10^6$ and the relative instability of the top centerline where transition occurs at $Re_x = 0.5 \times 10^6$ are of note. In contrast, transition on a 7 deg half-angle cone occurs at the intermediate value of $Re_x = 2.7 \times 10^6$ under similar test conditions in the same tunnel.[31,32] For the highest-Reynolds-number data the Stanton number profiles indicate that the flow is approaching a fully turbulent state, and the data follow the trend $C_H \propto Re_x^{-1/5}$.

Figure 9a shows the corresponding circumferential heat-transfer distributions over one quadrant of the cone at $x/L = 0.65$. Peak heating occurs at the leading edge and falls off toward the shoulder of the cone, a trend typical of laminar flows over blunt leading edges.[33] With transition we see the heat-transfer rate increase again and peak near the top centerline. For the lowest-Reynolds-number case ($Re_L = 1.7 \times 10^6$) transition begins at about $\theta = 30$ deg, whereas for the highest-Reynolds-number case ($Re_L = 6.7 \times 10^6$) transition begins around $\theta = 60$ deg.

Studies of low-speed, three-dimensional boundary-layer flows have shown that roughness-induced stationary disturbances can have a strong effect on transition.[17] The effect of roughness on the present flow was examined by attaching spheres to the surface of the cone upstream of the measurement station. Two circumferential configurations were tested: roughness elements of 2 mm diam and 1.3 mm diam spaced four diameters on center and distributed around one quadrant of the cone at $x/L = 0.225$. An additional configuration aligned along a ray was tested with 1.3-mm-diam elements affixed near the leading edge of the model ($\theta = 86$ deg) in a 0.165-mm strip centered at $x/L = 0.45$.

Because the roughness strips covered large regions of the model, the boundary-layer thickness varied along the strips. For the two circumferential configurations the ratio of roughness height to boundary-layer thickness at $\theta = 45$ deg was approximately $k/\delta = 0.4$ and 0.6 for the 1.3- and 2.0-mm-diam elements, respectively. The corresponding Reynolds numbers based on conditions at the top of the roughness elements were about $Re_k = 100$ and 400. For the configuration placed at $\theta = 86$ deg, the nondimensional roughness height was about $k/\delta = 0.7$ with $Re_k = 1100$.

Figure 9b shows the circumferential heat-transfer distribution at $x/L = 0.65$ and $Re_L = 1.7 \times 10^6$ with and without the roughness strips. Increased heat-transfer occurs in the range 20 deg $\leq \theta \leq$ 70 deg for the two cases in which the roughness elements were distributed around the circumference of the cone, and a double-peak feature in the heat-transfer distribution in the vicinity of $\theta = 45$ deg appears to amplify with increasing roughness diameter. In contrast, the roughness placed at the leading edge (not shown) did not have a detectable effect on the heat-transfer distribution.

The crossflow wavelength is expected to be approximately 13.7 mm (6.2 deg) at $\theta = 45$ deg and $x/L = 0.65$ (Ref. 24). Spacing on center for the 2- and 1.3-mm-diam roughness was 7.9 mm

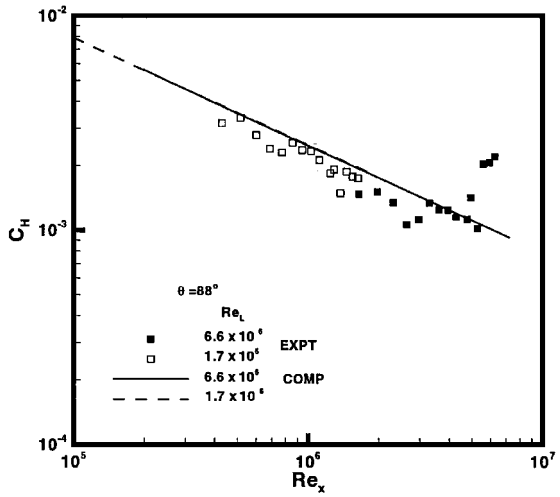

a) Leading edge, $\theta = 88$ deg

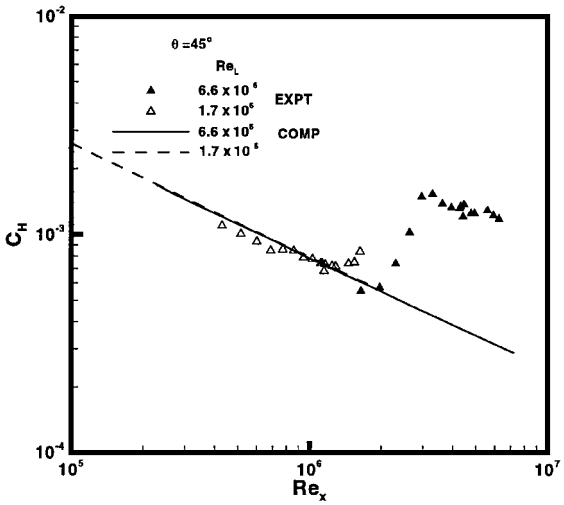

b) Shoulder, $\theta = 45$ deg

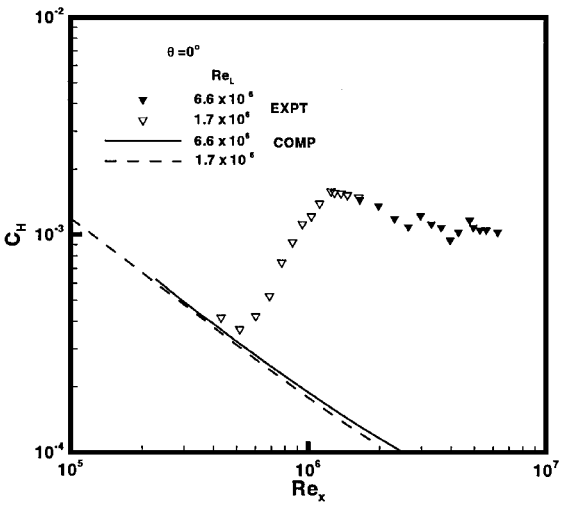

c) Top centerline, $\theta = 0$ deg

Fig. 8 Stanton number profiles along rays of the cone.

(3.2 deg) and 5.2 mm (1.8 deg), respectively. The five heat-transfer gauges in the range 38 deg $\leq \theta \leq$ 52 deg are spaced at 3.5-deg intervals. Heat-transfer data from these transducers show a circumferential periodicity of about 7 deg. Given these results, the temptation is to claim agreement between the circumferential period in the data and the crossflow wavelength, but the circumferential transducer spacing is near the Nyquist wave number, and the possibility exists for bias error, given that the measurements were not repeated with

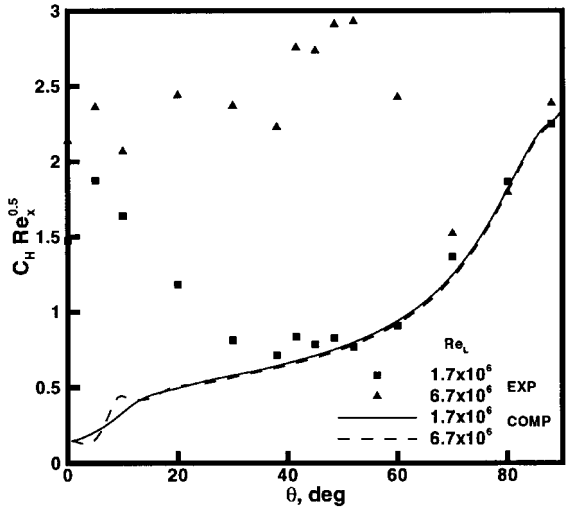

a) Baseline case

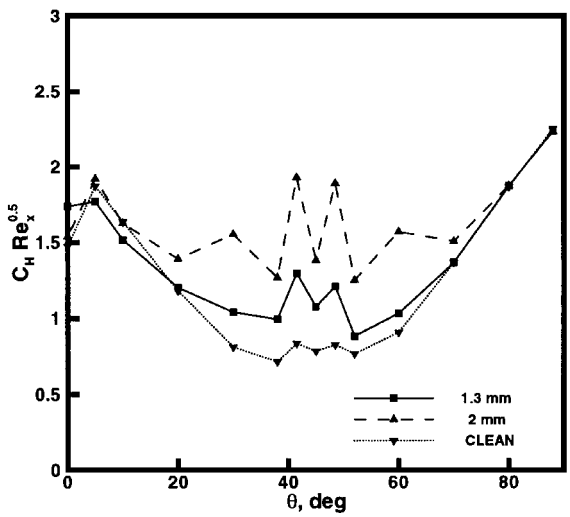

b) Roughness effects ($Re_L = 1.7 \times 10^6$)

Fig. 9 Stanton number profiles around the circumference of the cone for $x/L = 0.65$.

different transducers. Nevertheless, the fact that the heat-transfer pattern persists and amplifies with increasing roughness diameter (regardless of the circumferential spacing of the roughness) is suggestive of a stationary crossflow vortex signature.

Further, the roughness placed at the leading edge had essentially no effect on heat transfer at this station. Linear stability calculations[24] indicate that stationary crossflow vortices will have their axes aligned with the boundary-layer edge streamlines. The greater sensitivity of the flow to the circumferential roughness distribution than to the leading-edge roughness distribution suggests that disturbances engendered by the roughness elements propagated along the same directions as the crossflow vortices, rather than the surface streamlines.

Contours of Stanton number C_H as a function of Re_x and θ were constructed with data obtained at each of the freestream unit Reynolds numbers tested, assuming similarity with Reynolds number. The results are shown in Fig. 10. Discontinuities in heat transfer at $Re_x = 1.0 \times 10^6$ and 4.8×10^6 are artifacts of sparse transducer coverage of these regions. A maximum in the heat-transfer rate is seen at the leading edge ($\theta = 90$ deg), and a local maximum in heat transfer around the circumference of the model indicates boundary-layer transition. Transition occurs first on the top centerline of the cone and is very much delayed along the leading edge, in qualitative agreement with the pattern observed in the surface flow visualization of Fig. 5b.

To quantify the transition location, the measured heat transfer was divided by the calculated laminar-flow heat transfer to obtain a

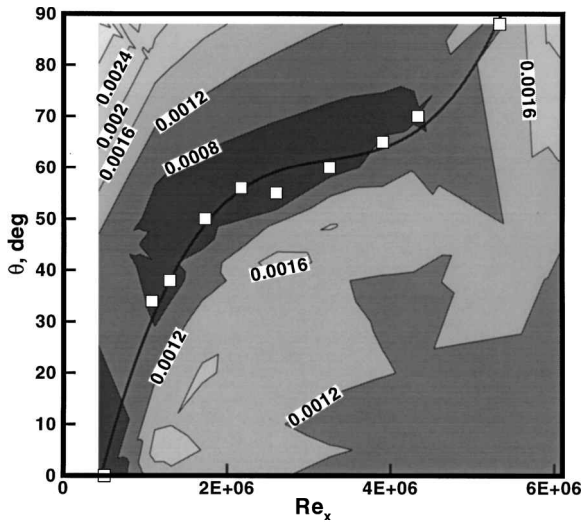

Fig. 10 Stanton-number contours: □, measured transition front; and ——, polynomial fit to data.

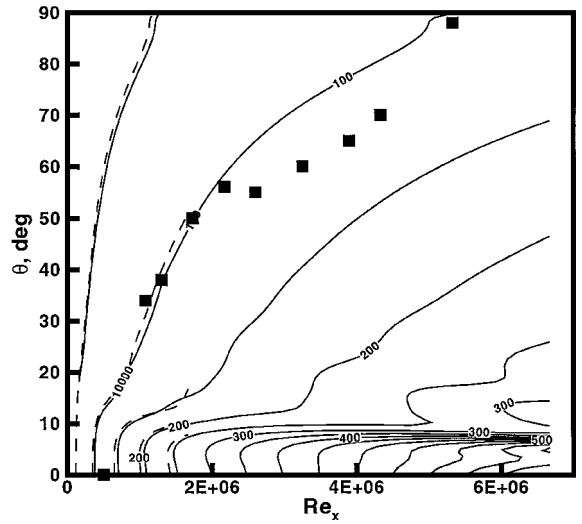

Fig. 11 Experimental transition front compared to contours of Re_θ/M_e: ■, measured transition front; – – –, Re_θ/M_e for $Re_L = 1.7 \times 10^6$; and ——, Re_θ/M_e for $Re_L = 6.7 \times 10^6$.

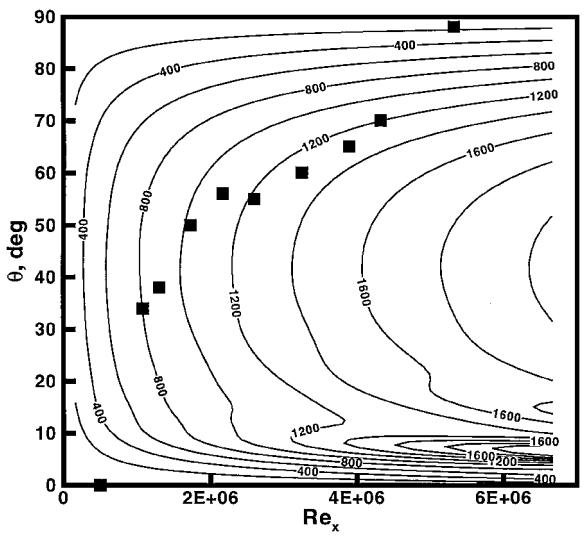

Fig. 12 Experimental transition front compared to contours of crossflow Reynolds number: ■, measured transition front; and ——, Re_{cf} for $Re_L = 6.7 \times 10^6$.

ratio r, which was near unity for laminar flow and greater than unity for turbulent flow. A threshold of $r = 1.5$ was chosen to indicate transition. This threshold is arbitrary, but the transition location was found to be relatively insensitive to the level of the threshold. Square symbols indicate in the figure the locations where the transition front defined in this fashion intercepted a ray or arc of heat-transfer gauges (see Fig. 2) at a given unit Reynolds number. A third-order, least-squares polynomial was fitted through these data and is indicated by the solid line in Fig. 10.

Despite the fundamental limitations inherent in correlations based on local basic state conditions, these correlations are still widely used in the design of aerospace vehicles because there is a compelling need for simple tools for preliminary design. One of the most commonly used criteria states that transition occurs when the ratio of local momentum thickness Reynolds number to the local edge Mach number exceeds some threshold value, typically $Re_\theta/M_e = 100$–300. Numerous researchers have pointed out the shortcomings of the Re_θ/M_e correlation. In an axisymmetric cone flow, for example, Re_θ goes as the square root of x, and M_e is nearly constant, so that a factor of three uncertainty in the threshold of Re_θ/M_e corresponds to a factor of nine uncertainty in transition location.[34] Crossflow Reynolds number Re_{cf} has also been used to correlate three-dimensional boundary-layer transition at various Mach numbers.[35] A modification to the crossflow Reynolds number has been proposed to take into account Mach number and wall-temperature effects,[36] but this correlation has been shown to be equivalent to Re_θ/M_e, at least for the present configuration.

Given the popularity of correlations based on local flow parameters, comparing the transition front measured in the elliptic cone flow to the Re_θ/M_e and crossflow correlations was considered useful. The results show a surprisingly good correlation between $Re_\theta/M_e =$ 100–150 and the measured transition location (Fig. 11). This result cannot, of course, be extrapolated to flight conditions or other geometric configurations. It does, however, indicate that Re_θ/M_e can perhaps take into account qualitative trends in the three-dimensional transition front. No single value of Re_{cf} correlates with the measured transition front (Fig. 12), as might be expected in a configuration with pronounced traveling wave instabilities on the leading edge and centerline. Around the shoulder of the model (40 deg $\leq \theta \leq$ 70 deg) where crossflow is strongest, the measured transition front lies between $Re_{cf} = 1000$ and 1200.

The flow in the vicinity of the leading edge of the cone seems to be highly stable, with the measured transition front shifted far downstream relative to other stations around the cone's circumference. Work at lower speeds[17] has indicated that attachment-line boundary layers are usually very stable in the absence of contamination from other parts of the flow. The leading-edge Reynolds number Re_D at transition was 6.8×10^5. Leading-edge transition on swept cylinders without end plates in hypersonic flow has been measured[37–39] at $Re_D = 8 \times 10^5$–12×10^5. (Measurements[40] at Mach 3.5 showed transition on swept cylinders without end plates to occur at $Re_D = 7 \times 10^5$–8×10^5, with little effect of wind-tunnel noise.) Leading-edge transition on the elliptic cone thus appears to be predicted by traditional leading-edge transition correlations.

Conclusions

To examine the influence of crossflow on transition from laminar to turbulent flow in a hypersonic boundary layer, an experimental and computational study was carried out in a Mach 8 flow over a cone of 2:1 elliptic cross section. Experimental data included flow visualization and surveys of the mean pressure and heat flux at the cone surface. A computation of the laminar basic state flow was carried out using the parabolized Navier–Stokes equations. The basic state laminar flow itself was found to be relatively complex, with highly skewed velocity profiles and a pair of symmetric vortices on the top centerline of the cone. The transition process was significantly different from that observed in previous studies of configurations with planar and axial symmetry where the second mode is typically the dominant instability.

The transition front was found to be nonuniform. Concomitant with the thick boundary layer and inflectional velocity profiles in

the vicinity of the top centerline was the earliest appearance of boundary-layer transition relative to other stations around the circumference of the cone. The flow in the vicinity of the leading edge of the cone appeared to be highly stable with the measured transition front shifted far downstream relative to other stations around the cone's circumference.

Transition on the top centerline may be related to an instability of the inflectional boundary-layer velocity profiles in that region, and a traveling crossflow instability is probably important in the vicinity of the shoulder of the cone. Some tentative evidence of stationary crossflow vortices was obtained when artificial roughness elements were placed around the circumference of the cone.

The present work has documented the overall features of transition in the elliptic cone flow and represents a first step toward understanding the transition process on relatively complex configurations in hypersonic flow. Much additional work is needed before accurate computations of transition location can be made for this class of flows. In particular, little is known about the receptivity process by which external disturbances are transformed into the initial perturbations in the boundary-layer flow. One promising avenue of receptivity research is the use of controlled disturbances in quiet wind-tunnel facilities. Quiet facilities also offer the possibility of determining transition Reynolds numbers that can be extrapolated to flight conditions with reasonable accuracy. Additional experimentation on the elliptic cone configuration in such a facility is warranted.

Acknowledgments

This project was sponsored by the U.S. Air Force Office of Scientific Research and monitored by L. Sakell and S. Walker. J. Donaldson, C. Nelson, A. Davenport, and co-workers at Sverdrup Technology, Inc., supported the experimental component of this project.

References

[1]Mack, L. M., "Linear Stability Theory and the Problem of Supersonic Boundary Layer Transition," *AIAA Journal*, Vol. 13, No. 3, 1975, pp. 278–289.

[2]Mack, L. M., "Boundary-Layer Linear Stability Theory," *Special Course on Stability and Transition of Laminar Flow*, edited by R. Michel, R-709, AGARD, 1984, pp. 3-1–3-81.

[3]Mack, L. M., "On the Inviscid Acoustic-Mode Instability of Supersonic Shear Flows, Part 1: Two-Dimensional Waves," *Theoretical and Computational Fluid Dynamics*, Vol. 2, No. 1, 1990, pp. 97–123.

[4]Balakumar, P., and Malik, M. R., "Waves Produced from a Harmonic Point Source in a Supersonic Boundary-Layer Flow," *Journal of Fluid Mechanics*, Vol. 245, 1992, pp. 229–247.

[5]Pruett, C. D., and Chang, C.-L., "Spatial Direct Numerical Simulation of High-Speed Boundary-Layer Flows, Part II: Transition on a Cone in Mach 8 Flow," *Theoretical and Computational Fluid Dynamics*, Vol. 7, No. 5, 1995, pp. 397–424.

[6]Zhong, X., "Direct Numerical Simulation of Hypersonic Boundary-Layer Transition over Blunt Leading Edges, Part II: Receptivity to Sound," AIAA Paper 97-0756, Jan. 1997.

[7]Demetriades, A., "An Experiment on the Stability of Hypersonic Laminar Boundary Layers," *Journal of Fluid Mechanics*, Vol. 7, No. 3, 1960, pp. 385–396.

[8]Kendall, J. M., "Wind Tunnel Experiments Relating to Supersonic and Hypersonic Boundary-Layer Transition," *AIAA Journal*, Vol. 13, No. 3, 1975, pp. 290–299.

[9]Stetson, K. F., and Kimmel, R. L., "On Hypersonic Boundary-Layer Stability," AIAA Paper 92-0737, Jan. 1992.

[10]Kimmel, R. L., Demetriades, A., and Donaldson, J. C., "Space-Time Correlation Measurements in a Hypersonic Transitional Boundary Layer," *AIAA Journal*, Vol. 34, No. 12, 1996, pp. 2484–2489.

[11]Lachowicz, J. T., Chokani, N., and Wilkinson, S. P., "Boundary-Layer Stability Measurements in a Hypersonic Quiet Tunnel," *AIAA Journal*, Vol. 34, No. 12, 1996, pp. 2496–2500.

[12]Malik, M. R., "Prediction and Control of Transition in Supersonic and Hypersonic Boundary Layers," *AIAA Journal*, Vol. 27, No. 11, 1989, pp. 1487–1493.

[13]Wendt, V., Simen, M., and Hanifi, A., "An Experimental and Theoretical Investigation of Instabilities in Hypersonic Flat Plate Boundary Layer Flow," *Physics of Fluids*, Vol. 7, No. 4, 1995, pp. 877–887.

[14]Kimmel, R. L., and Poggie, J., "Disturbance Evolution and Breakdown to Turbulence in a Hypersonic Boundary Layer: Ensemble-Averaged Structure," AIAA Paper 97-0555, Jan. 1997.

[15]Poggie, J., and Kimmel, R. L., "Disturbance Evolution and Breakdown to Turbulence in a Hypersonic Boundary Layer: Instantaneous Structure," AIAA Paper 97-0556, Jan. 1997.

[16]Smits, A. J., and Dussauge, J.-P., *Turbulent Shear Layers in Supersonic Flow*, American Inst. of Physics, Woodbury, NY, 1996.

[17]Reed, H. L., and Saric, W. S., "Stability of Three-Dimensional Boundary Layers," *Annual Review of Fluid Mechanics*, Vol. 21, 1989, pp. 235–284.

[18]Stetson, K. F., Thompson, E. R., Donaldson, J. C., and Siler, L. G., "Laminar Boundary Layer Stability Experiments on a Cone at Mach 8, Part 3: Sharp Cone at Angle of Attack," AIAA Paper 85-0492, Jan. 1985.

[19]Doggett, G. P., Chokani, N., and Wilkinson, S. P., "Effect of Angle of Attack on Hypersonic Boundary Layer Stability," *AIAA Journal*, Vol. 35, No. 3, 1997, pp. 464–470.

[20]Burke, G. L., "Heat Transfer and Pressure Distributions About Sharp and Blunt Elliptic Cones at Angles of Attack and High Mach Numbers," U.S. Air Force Flight Dynamics Lab., TR AFFDL-TR-64-172, Wright–Patterson AFB, OH, May 1965.

[21]Malik, M., and Balakumar, P., "Instability and Transition in Three-Dimensional Supersonic Boundary Layers," AIAA Paper 92-5049, Dec. 1992.

[22]Balakumar, P., and Reed, H. L., "Stability of Three-Dimensional Supersonic Boundary Layers," *Physics of Fluids A*, Vol. 3, No. 4, 1991, pp. 617–632.

[23]Kimmel, R. L., Klein, M. A., and Schwoerke, S. N., "Three-Dimensional Hypersonic Laminar Boundary-Layer Computations for Transition Experiment Design," *Journal of Spacecraft and Rockets*, Vol. 34, No. 4, 1997, pp. 409–415.

[24]Poggie, J., Kimmel, R. L., and Schwoerke, S. N., "Traveling Instability Waves in a Mach 8 Flow over an Elliptic Cone," *AIAA Journal* (to be published).

[25]"Von Kármán Gas Dynamics Facility," *Test Facilities Handbook*, Vol. 3, 11th ed., Arnold Engineering Development Center, Arnold AFB, TN, 1981.

[26]Boudreau, A. H., "Performance and Operational Characteristics of AEDC/VKF Tunnels A, B, and C," Arnold Engineering Development Center, TR AEDC-TR-80-48 (ADA102614), Arnold AFB, TN, July 1981.

[27]Donaldson, J. C., and Coulter, S. M., "A Review of Free-Stream Flow Fluctuation and Steady-State Flow Quality Measurements in the AEDC/VKF Supersonic Tunnel A and Hypersonic Tunnel B," AIAA Paper 95-6137, April 1995.

[28]Lyttle, I. J., and Reed, H. S., "Use of Transition Correlations for Three-Dimensional Boundary Layers Within Hypersonic Flows," AIAA Paper 95-2293, June 1995.

[29]Lyttle, I. J., and Reed, H. S., "Use of Transition Correlations for Three-Dimensional Boundary Layers Within Hypersonic, Viscous Flows," *Transitional and Turbulent Compressible Flows*, ASME Fluids Engineering Div., Vol. 224, American Society of Mechanical Engineers, New York, 1995, pp. 87–94.

[30]Lawrence, S. L., Tannehill, J. C., and Chaussee, D. S., "An Upwind Algorithm for the Parabolized Navier–Stokes Equations," AIAA Paper 86-1117, May 1986.

[31]Mack, L. M., "Boundary-Layer Stability Analysis for Sharp Cones at Zero Angle-of-Attack," U.S. Air Force Wright Aeronautical Lab., TR AFWAL-TR-86-3022, Wright–Patterson AFB, OH, Aug. 1986.

[32]Kimmel, R. L., "The Effect of Pressure Gradients on Transition Zone Length in Hypersonic Boundary Layers," *Journal of Fluids Engineering*, Vol. 119, March 1997, pp. 36–41.

[33]Anderson, J. D., *Hypersonic and High Temperature Gas Dynamics*, McGraw–Hill, New York, 1989.

[34]Stetson, K. F., "On Predicting Hypersonic Boundary Layer Transition," U.S. Air Force Wright Aeronautical Lab., TM AFWAL-TM-87-160-FIMG, Wright–Patterson AFB, OH, March 1987.

[35]Pate, S. R., "Dominance of Radiated Aerodynamic Noise on Boundary-Layer Transition in Supersonic-Hypersonic Wind Tunnels, Theory and Application," Arnold Engineering Development Center, TR AEDC-TR-77-107, Arnold AFB, TN, March 1978.

[36]Reed, H. L., and Haynes, T. S., "Transition Correlations in Three-Dimensional Boundary Layers," *AIAA Journal*, Vol. 32, No. 5, 1994, pp. 923–929.

[37]Bushnell, D. M., and Huffman, J. K., "Investigation of Heat Transfer to Leading Edge of a 76° Swept Fin With and Without Chordwise Slots and Correlations of Swept-Leading-Edge Transition Data for Mach 2 to 8," NASA TM-X-1475, Dec. 1967.

[38]Murakami, A., Stanewsky, E., and Krogmann, P., "Boundary Layer Transition on Swept Cylinders at Hypersonic Speeds," AIAA Paper 95-2276, June 1995.

[39]Holden, M., and Kolly, J., "Attachment Line Transition Studies on Swept Cylindrical Leading Edges at Mach Numbers from 10 to 12," AIAA Paper 95-2279, June 1995.

[40]Creel, T. R., Jr., Beckwith, I. E., and Chen, F. J., "Transition on Swept Leading Edges at Mach 3.5," *Journal of Aircraft*, Vol. 24, No. 10, 1987, pp. 710–717.

P. Givi
Associate Editor